Journal of Chromatography A, 1222 (2012) 46–58

Contents lists available at SciVerse ScienceDirect

Journal of Chromatography A

journal homepage: www.elsevier.com/locate/chroma

Morphology and separation efficiency of a new generation of analytical silica monoliths

Kristof Hormann, Tibor Müllner, Stefan Bruns, Alexandra Höltzel, Ulrich Tallarek*

Department of Chemistry, Philipps-Universität Marburg, Hans Meerwein Strasse, 35032 Marburg, Germany

ARTICLE INFO

Article history:
Received 16 September 2011
Received in revised form 1 December 2011
Accepted 4 December 2011
Available online 9 December 2011

Keywords:
Analytical silica monoliths
Physical reconstruction
Morphological analysis
Chord length distribution
Radial heterogeneity
Eddy dispersion

ABSTRACT

The heterogeneous morphology of current silica monoliths hinders this column type to reach its envisioned performance goals. We present a new generation of analytical silica monoliths that deliver a substantially improved separation efficiency achieved through several advances in monolith morphology. Analytical silica monoliths from the 1st and 2nd Chromolith generation are characterized and compared by chromatographic methods, mercury intrusion porosimetry, scanning electron microscopy, and confocal laser scanning microscopy. The latter method is instrumental to quantify morphological differences between the monolith generations and to probe the radial variation of morphological properties. Compared with the 1st generation, the new monoliths possess not only smaller macropores, a more homogeneous macropore space, and a thinner silica skeleton, but also radial homogeneity of these structural parameters as well as of the local external or macroporosity. The 66.5% reduction in minimum plate height observed between silica monoliths of the 1st and 2nd Chromolith generation can thus be attributed to two key improvements: a smaller domain size at simultaneously increased macropore homogeneity and the absence of radial morphology gradients, which are behind the considerable peak asymmetry of the 1st generation.

1. Introduction

Innovative chromatographic supports introduced to a wider community in the last decade are silica and organic polymer-based monoliths [1–12], solid core–porous shell particles [13,14], and sub-2 μm particles [15,16]. The latter two particle types have aroused enthusiasm for enabling outstanding separation efficiencies, while the strength of organic-polymer based monoliths is their versatility. Against this scenario, silica-based monoliths have retreated into the background. This is an undeserved fate, because the potential of silica monoliths is undisputed: to deliver the approved stationary phase chemistry of 3.5 or 5-μm sized porous silica particles, but at enhanced separation efficiency and higher column permeability [17–25]. The morphological concept of a bimodal structure made of mesoporous silica skeleton perforated by flow-through macropores (∼2 μm diameter) enables a mechanically stable bed at high external porosity (macroporosity, $\varepsilon_{ext} \approx 0.7$), which translates to a permeability comparable to that of columns packed with 11-μm particles in the porosity range of mechanically stable particulate beds ($\varepsilon_{ext} = 0.38$–0.42) [17,20]; the high permeability enables short analysis times, serving the demands of high-throughput screening applications. The thin skeleton (∼1 μm) ensures short diffusion pathways, reducing the mass transfer contribution to band broadening. Short diffusion pathways are also the original concept behind solid core–porous shell particles [14]; in contrast to shell particles, however, silica monoliths have so far not lived up to their potential, considering the separation efficiencies envisioned for them [4]. This is all the more vexing, because – in the quest of combining high separation efficiency with high permeability – even the ingenious shell particles cannot improve column permeability to the point of monolithic beds.

Silica monoliths suffer from a large eddy dispersion contribution to band broadening, originating from flow velocity inequalities at various scales [26]. These are (from smaller to larger): a transskeleton velocity bias across the thickness of the mesoporous skeleton, a transchannel velocity bias across the size of a macropore, a short-range interchannel velocity bias at the scale of one domain size (the sum of average macropore size and average skeleton thickness), and a transcolumn velocity bias over the whole column cross-section. Gritti and Guiochon [26] have identified three drawbacks of silica monolith morphology: (1) the large size distribution, variable geometry, and random spatial distribution of the macropores; (2) the large domain size,

* Corresponding author. Tel.: +49 6421 28 25727; fax: +49 6421 28 27065.
E-mail address: tallarek@staff.uni-marburg.de (U. Tallarek).
URL: http://www.uni-marburg.de/fb15/ag-tallarek (U. Tallarek).

0021-9673/$ – see front matter © 2011 Elsevier B.V. All rights reserved.
doi:10.1016/j.chroma.2011.12.008

which has not kept up with the ever downsizing diameters of porous silica particles; and (3) a radially heterogeneous morphology. Heterogeneity of the macropore space affects the short-range interchannel velocity bias, a larger macropore size and skeleton thickness increase the transschannel and transskeleton velocity bias, respectively, and radial heterogeneity of the morphology the transcolumn velocity bias. The radial heterogeneity is supposed to stem from chemical and/or temperature gradients that form across the column bed during the monolith preparation [4]. Also, strain resulting from the stress caused by the shrinkage of the monolithic rod after formation of a solid network may cause the interface between monolith and column wall to break due to inelastic deformations. Then, the monolith can separate from the wall causing slightly higher local porosities in the wall region. By placing electrochemical detectors at various points of the cross-section at the column exit of semi-preparative (10 mm i.d.) and analytical (4.6 mm i.d.) silica monoliths, Guiochon and co-workers [27,28] found 4% and 1.5% velocity difference, respectively, between wall and core region. Even at only a few percent, morphological differences, *e.g.*, in the local macroporosity, cause a noticeable loss of separation efficiency. Another, severe form of radial heterogeneity occurs in capillary monoliths: as opposed to larger-diameter monolithic rods, capillary monoliths are prepared directly in the tube then used for chromatographic separations; the persistent mechanical stress introduced by the shrinking may cause the bed to snap back from the rigid column wall, yielding gaps that allow the mobile phase to bypass the bed [29]. Efforts directed against this problem have been published recently [30–34].

Successful strategies to decrease the domain size were already worked out earlier by Tanaka's group [35–38]. They prepared monolithic columns (7 mm i.d.) with domain sizes of 5.9–2.3 μm and obtained minimum plate heights of H_{min} = 5–10 μm [36], and a minimum plate height of H_{min} = 5 μm was achieved for a capillary monolith with a domain size of 2.2 μm [38]. Because further reduction of the domain size failed to improve separation efficiency, it was speculated that below a certain domain size the structural self-similarity of the monolith breaks down, *i.e.*, the homogeneity of the morphology deteriorates. But whether this is a fundamental property of silica monoliths or a problem that could be overcome by appropriate preparation methods, has not been answered yet [25]. One reason may be the relative scarcity of published silica monolith preparations, another is the difficulty of retrieving relevant morphological information: whereas average properties such as the domain size or porosities are easily accessible, assessing the structural heterogeneity of a column or detecting a systematic radial variation of morphological properties is not straightforward.

The usually offered scanning electron microscopy (SEM) images of cross-sectional cuts of a column provide an overview of the morphology, but because SEM offers no depth information, it cannot produce reliable quantitative information. Transmission electron microscopy (TEM), on the other hand, delivers quantifiable depth information at nanometer resolution and thus the desired morphological information, but the technique is neither as widely and easily accessible as SEM nor as fast and comfortable [39]. TEM requires slices of < 0.5 μm thickness, which are cut from the sample and polished before examination. The morphology of the sample, *e.g.*, a piece of monolithic rod, can be physically reconstructed from successive TEM slices, but the reconstructed sample volume needs to be sufficiently large to extract the desired morphological information, which makes obtaining the requisite number of sequential, undamaged slices an ambitious project. A recently developed technique, serial block-face scanning electron microscopy, overcomes this obstacle through a combination of fully automated SEM imaging and *in situ* ultramicrotomy [40]. This method has been used for the three-dimensional reconstruction of porous polymer structures [41,42]. However, it is not applicable to silica monoliths as the diamond knife of the ultramicrotome would not withstand the cutting process.

Contrary to SEM and TEM, non-destructive methods such as nuclear magnetic resonance (NMR) imaging [43–45], micro-X-ray tomography [46–49], and capacitively coupled contactless conductivity detection (C^4D) [50–52] do not require cutting the column into slices. NMR imaging has a resolution on the order of tens of μm, which makes this technique better suited for beds of larger (up to mm-sized) particles. Micro-X-ray tomography has excellent resolution, but only for small sample volumes, which may be insufficient to represent the bulk material and its properties. C^4D allows quick scanning for large heterogeneities, *e.g.*, gaps along a column's whole length, but cannot detect radial heterogeneity; it yields a scalar value representing the silica density over the column's cross-section and therefore does not allow to reconstruct the material's microstructure.

Confocal laser scanning microscopy (CLSM) [53], where the laborious physical slicing is replaced by optical slicing, offers an easier way to visualize the macromorphology of silica monoliths. Although inferior in resolution to SEM and TEM, CLSM can be used to generate comparable quantitative morphological information. Jinnai and co-workers [54–58] published three-dimensional reconstructions of custom-prepared silica-based monoliths. They studied monolithic samples not in a column format, but either unconfined or confined between two cover slips. The three-dimensional reconstructions gave insight into the formation process of monoliths and their geometrical properties like pore shape and connectivity.

We recently introduced a CLSM-based approach consisting of column pretreatment, image acquisition, processing, and analysis, for the physical reconstruction of the morphology of silica monolithic as well as silica-based particulate columns in capillary format [59,60]. The small inner diameter of capillary columns is compatible with the penetration depth of the technique, which enables direct CLSM imaging of these columns over the whole column cross-section. Quick scanning of capillary monoliths for longitudinal heterogeneities is possible, but the real strength of the method lies in providing detailed information about radial variations in the column morphology. In this contribution, we apply our CLSM-approach to silica monoliths in analytical column format. Because the larger inner diameter (4.6 mm) prohibits direct CLSM imaging of the columns, we use sample pieces, cylindrical disks of ~1 mm thickness cut from the monolithic rods. The necessary step of slicing eliminates the possibility to detect longitudinal morphological heterogeneities, but in this contribution we focus on the radial heterogeneity and the general morphological properties. The monolith macromorphology is physically reconstructed at several positions of a sample disk and quantitative morphological information is derived from the reconstructed volumes in form of chord length distributions for macropore space and silica skeleton. We use this information to detect the morphological differences between two generations of commercial, analytical silica monoliths: the 1st monolith generation has been sold as Chromolith Performance columns by Merck since 2000, and the 2nd generation was announced at the HPLC 2011 conference in Budapest to be introduced to the market as Chromolith High-Resolution columns. We investigate Chromolith columns from the 1st and 2nd generation by chromatographic methods, mercury intrusion porosimetry (MIP), SEM, and CLSM, and use the combined results to identify relevant morphological advances made with the 2nd generation monoliths and to explain the consequences for separation efficiency.

2. Materials and methods

2.1. Chemicals and materials

Laboratory samples of 1st and 2nd generation Chromolith columns were received from Merck Millipore (Darmstadt, Germany) as bare-silica rods (4.6 mm × 150 mm) and as C_{18}-modified, fully end-capped, analytical HPLC columns (4.6 mm × 100 mm) clad in polyether ether ketone (PEEK). The preparation of the Chromolith columns is based on an established procedure described in more detail in [61] and references therein.

3-Carboxy-6-chloro-7-hydroxycoumarin (dye V450) was purchased from Endotherm Life Science Molecules (Saarbrücken, Germany). 3-Aminopropyl-triethoxysilane (APTES), N,N′-disuccinimidyl carbonate (DSC), and 4-dimethylaminopyridine (DMAP) were provided by Alfa Aesar (Karlsruhe, Germany). Triethylamine (TEA), dimethyl sulfoxide (DMSO), dimethylformamide (DMF), glycerol, and HPLC-grade methanol, ethanol, and acetonitrile (ACN) were supplied by Sigma–Aldrich Chemie (Taufkirchen, Germany). 2-Amino-2-hydroxymethyl-propane-1,3-diol (Tris), butylbenzene, and thiourea were from Fluka (Steinheim, Germany), HCl from VWR International (Darmstadt, Germany), and KNO_3 from Carl Roth (Karlsruhe, Germany). HPLC-grade water was obtained from a Milli-Q gradient water purification system (Millipore, Bedford, MA).

2.2. Liquid chromatography

Chromatographic experiments with the PEEK-clad, C18-modified and fully endcapped, analytical columns were carried out on an Agilent 1100 liquid chromatograph (Agilent Technologies, Waldbronn, Germany) equipped with a degasser, a binary solvent pump, an auto-sampler, and an UV transmission detector. Plate height curves and pressure drop–flow rate data were acquired with a mobile phase of water/ACN 40/60 (v/v) at flow rates between 0.2 and 4 mL/min. The flow rate was monitored at the detector outlet by a digital flow meter based on photoelectric barrier time measurement (Model 4085, Alltech Associates, Deerfield, IL). 1 μL of the sample containing 0.07 mg/mL thiourea (dead time marker) and 0.1 mg/mL butylbenzene (analyte) was injected. The detection wavelength was 254 nm. Plate heights were determined from the peak width at half-height via the ChemStation software (Agilent Technologies, Waldbronn, Germany) and from the peak's statistical moments following the protocol of Gritti and Guiochon [62,63], using an in-house MATLAB script (MathWorks, Natick, MA) for total numerical peak integration. For the latter method, chromatograms were baseline-corrected and extra-column contributions to band broadening were determined from peak profiles measured in the presence of a zero-dead-volume union connector which replaced the monolithic column.

The total porosity of the columns was determined from the elution volume of thiourea in a mobile phase of water/ACN 20/80 (v/v) at a flow rate of 0.5 mL/min.

For electrostatic (Donnan) exclusion chromatography a mobile phase of water/ACN 50/50 (v/v) containing Tris–HCl buffer (pH 8.1) at concentrations between 0.01 and 60 mmol/L was used. The flow rate was 0.5 mL/min, and KNO_3 was used as analyte and detected at a wavelength of 210 nm. Samples (injected volume: 1 μL) were prepared to match the ionic strength of the mobile phase. For concentrations between 0.01 and 0.04 mmol/L, KNO_3 solutions in pure water were used, while for higher concentrations, KNO_3 solutions contained 0.04 mmol/L Tris–HCl buffer. Columns were purged, until the retention volume of the analyte was constant, which took between 1 and 2 h per eluent composition.

2.3. Mercury intrusion porosimetry

Porosimetry measurements of bare-silica monolithic rods were made with a PoreMaster 60 (Quantachrome Instruments, Boynton Beach, FL). A pressure range of 1.5–4000 bar (0.15–400 MPa) was sampled. According to the well-known Washburn equation

$$p = \frac{4\,\gamma\,\cos\,\theta}{d_{pore}}, \quad (1)$$

where p is the applied pressure, γ the surface tension of mercury, θ the contact angle of mercury on a silica surface, and d_{pore} the pore diameter, the measured pressure range corresponds to pore diameters between 3.7 nm and 10 μm. The mercury density was 13.5 g/cm^3 at 293 K, and a contact angle of θ = 140° was assumed (mercury–air surface tension at 293 K: γ = 486.5 mN/m) [25].

2.4. Scanning electron microscopy

We used a JEOL JSM-7500F SE microscope (Tokyo, Japan). Fragments of the bare-silica monolithic rods were fixed on aluminum sample holders and electrically contacted using carbon conducting cement; a sputter coating was not applied. Micrographs were analyzed with ImageJ 1.42 software [64].

2.5. Confocal laser scanning microscopy

2.5.1. Synthesis of dye V450 succinimidyl ester

We followed the approach described by Abrams et al. [65] and outlined in Bruns et al. [59]. 40.2 mg dye V450 were dissolved in 3 mL DMF containing 48 μL TEA and 1.4 mg DMAP. Following addition of 83.7 mg DSC, the solution was stirred for 6 h at room temperature and afterwards concentrated *in vacuo*. The synthesis product was precipitated in 10 mL water, filtered, and dried at room temperature under reduced pressure. V450 succinimidyl ester was synthesized as white-yellowish solid with 65% yield.

2.5.2. Sample preparation

Cylindrical disks of 4.6 mm diameter and 1–1.5 mm thickness were cut at *ca.* mid-length from bare-silica monolithic rods orthogonal to the column axis using a water-cooled circular saw. Disks were washed with ethanol and dried at 50 °C and reduced pressure for 24 h. Surface modification and staining followed the approach that we reported previously [34,59,60] and is only briefly summarized here. For amine-modification of the bare-silica surface, each disk was immersed for 5 h in 5 mL of a 0.1 M solution of APTES in ethanol at 70 °C, and subsequently washed several times with ethanol and water/methanol (50/50, v/v). After purging with DMF, each disk was immersed for 6 h in 1 mL of a V450 succinimidyl ester solution in DMF (0.1 mg/mL). Excess dye (not covalently bound to the substrate) was removed by washing with DMF.

A ternary mixture of glycerol, DMSO, and water (70/19/11, v/v/v) was prepared to match the optical dispersion behavior of the silica skeleton over the wavelength range relevant for the measurements (400–480 nm) [59,60]. The refractive index of the ternary mixture was adjusted with an AR200 digital refractometer (Reichert Analytical Instruments, Depew, NY) to the refractive index of the silica skeleton at the sodium D line (n_D = 1.4582). Prior to image acquisition, the DMF-saturated stained silica disks were immersed in 1 mL of the matching liquid for 10 h, during which the solution was refreshed every 2 h.

2.5.3. Image acquisition

Images were acquired using a TCS SP5 II confocal microscopy system equipped with a HCX PL APO 63x/1.3 GLYC CORR CS (21°) glycerol immersion objective lens from Leica Microsystems

(Wetzlar, Germany). The sample was mounted directly underneath a cover slip by placing the stained cylindrical silica disk into the embedding liquid-filled well of a custom-made sample holder. A "type 0" cover slip (Gerhard Menzel GmbH, Braunschweig, Germany) was chosen to separate embedding and immersion liquid and minimize spherical aberrations [60]. The prepared matching liquid was used for immersion and embedding.

Fluorescence of the V450 dye (λ_{exc} = 404 nm, λ_{em} = 448 nm) was excited with a UV diode laser at 405 nm and detected in the interval of 425–480 nm. Sampling steps of 30 nm (lateral) and 126 nm (axial) were calculated using the Nyquist rate and point spread function calculator (Scientific Volume Imaging, Hilversum, The Netherlands). Stacks of 8-bit grayscale images of 2048 × 2048 pixels were acquired at arbitrarily chosen positions in the cylindrical plane of the disk, *i.e.*, perpendicular to the axis of the monolithic rod from which the disk was cut. For data collection a distance of at least 10 μm from the disk surface was maintained to avoid possible morphological distortions originating from the cutting process. The number of images per stack varied between 100 and 200.

For investigating the radial homogeneity of the monolith, 11 image stacks (dimensions as above) were acquired at approximately equidistant locations from close to (but not at) the edge of a disk to its center. These stacks were acquired at the same depth to eliminate the influence of longitudinal morphological heterogeneities on the measurement.

2.5.4. Image processing

Image processing consisted of four consecutive steps, whose details are described elsewhere [60]. (1) Images were corrected for the contribution of the Poisson-distributed photon noise using the PureDenoise plug-in for ImageJ [64] provided by Luisier [66]. (2) The acquired image stack was corrected for the intensity loss from photobleaching by fitting the average intensity of the images along the z-axis to a second-order exponential decay. (3) Images were deconvolved with the Huygens Maximum Likelihood Algorithm (Scientific Volume Imaging, Hilversum, The Netherlands). (4) Images were segmented by twice subtracting from the deconvolved image stack a copy of this stack blurred with a large Gaussian kernel filter (standard deviation: 200 pixels) to obtain a homogeneous background intensity corresponding to the intensity value zero. All pixels with an intensity value above zero were then assigned as skeleton. To eliminate artifacts from processing, image stacks were cropped in lateral dimension to 2000 × 2000 pixels and in axial dimension by discarding the five top and bottom images; each image stack subjected to image analysis corresponded to a physical volume of at least 60 μm × 60 μm × 12.6 μm.

2.5.5. Image analysis

The segmented image stacks were analyzed on the basis of chord length distributions (CLDs), as introduced by Courtois et al. [39], using in-house software written with Visual Studio C# 2008 (Microsoft Corporation, Redmond, WA). To calculate the CLD for the macropore space, points were randomly chosen from the void space of an image stack. From each point vectors were projected in 32 angularly equispaced directions, until they either hit the skeleton or projected out of the image boundaries; in the latter case, the corresponding vector pairs were discarded. Points of origin were chosen until the value of 62,500 was reached. Chord lengths were calculated as the sum of the absolute lengths of a pair of opposed vectors. The 10^6 collected chord lengths were binned using a bin size of 0.2 μm, and the resulting histogram was fitted to a k-gamma function using the Levenberg-Marquardt algorithm [67]. To calculate the CLD for the silica skeleton, points of origin were chosen in the solid space and vectors were projected towards the void space.

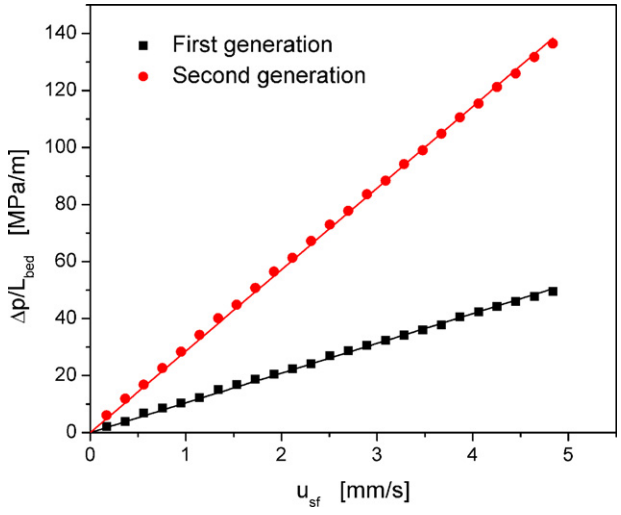

Fig. 1. Pressure drop–flow rate relation of 1st and 2nd generation Chromolith columns (4.6 mm × 100 mm, C_{18}-modified, fully end-capped). Pressure gradient as a function of the superficial velocity, mobile phase: 40/60 (v/v) water/ACN. Solid lines are best fits of the data to Eq. (2).

The macroporosity ε_{ext} of a reconstructed volume of the monolith macromorphology was calculated as the fraction of void pixels in the respective image stack.

3. Results and discussion

3.1. Chromatographic performance of analytical Chromolith columns

Figs. 1 and 2 summarize the chromatographic performance of silica monolith columns from the 1st and the 2nd Chromolith generation (Table 1). The data were acquired with C_{18}-modified and fully end-capped, PEEK-clad analytical columns (4.6 mm × 100 mm), a mobile phase of water/ACN 40/60 (v/v), thiourea as dead time marker and butylbenzene as analyte

Table 1
Chromatographic properties of C_{18}-modified, fully end-capped columns from the 1st and 2nd generation of analytical silica monoliths.

	1st	2nd	Ratio (2nd/1st)
K_D (×10^{-14} m^2)	7.38	2.68	0.36
Symmetry factor[a]	0.64	0.80	1.25
H_{min} (μm)[b]	11.0	6.7	0.61
$u_{av,min}$ (mm/s)[b]	1.76	1.91	1.09
A (μm)[b]	6.19	2.42	0.39
B (×10^3 μm^2/s)[b]	4.27	4.06	0.95
C (×10^{-3} s)[b]	1.38	1.11	0.80
H_{min} (μm)[c]	21.8	7.3	0.33
$u_{av,min}$ (mm/s)[c]	0.50	1.79	3.58
A (μm)[c]	16.6	3.9	0.23
B (×10^3 μm^2/s)[c]	1.3	3.1	2.38
C (×10^{-3} s)[c]	5.2	1.0	0.19
ε_{tot}[d]	0.81	0.81	1.00
ε_{ext}[e]	0.64	0.62	0.97
$\varepsilon_{int,col}$[f]	0.17	0.19	1.12
$\varepsilon_{int,skel}$[g]	0.47	0.50	1.06

[a] Calculated as a pseudomoment by the Agilent ChemStation software.
[b] Fitted with Eq. (5), based on plate height data obtained from the FWHM of the butylbenzene peak.
[c] Fitted with Eq. (5), based on plate height data calculated with the statistical moments after numerical integration of the butylbenzene peak, cf. Eq. (4).
[d] From the elution volume of the unretained tracer thiourea.
[e] From electrostatic (Donnan) exclusion chromatography of KNO_3 (nitrate ions).
[f] Calculated with Eq. (6).
[g] Calculated with Eq. (7).

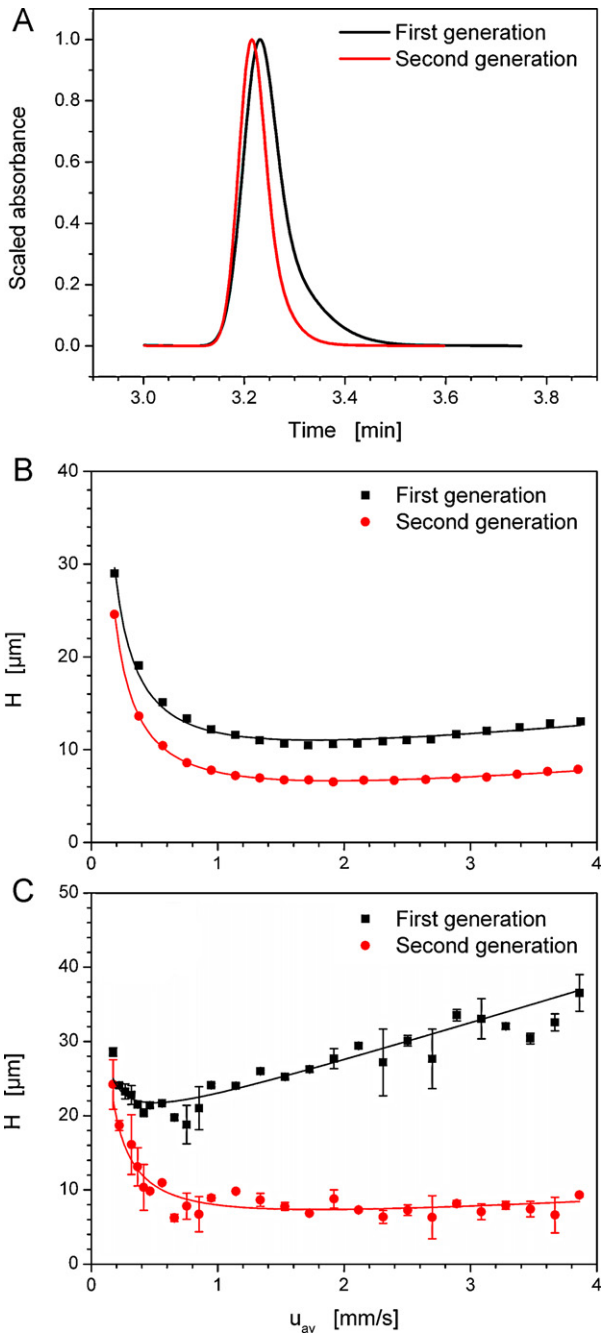

Fig. 2. Separation efficiency of 1st and 2nd generation Chromolith columns (4.6 mm × 100 mm, C_{18}-modified, fully end-capped). Mobile phase: 40/60 (v/v) water/ACN. (A) Chromatograms of butylbenzene, scaled to a maximum absorbance of 1.0. (B) Plate height data determined from the full width at half maximum of the butylbenzene peak. (C) Plate height data determined from the peak's statistical moments after numerical integration of the butylbenzene peak. Solid lines in panels (B) and (C) are best fits of the data to Eq. (5).

(retention factor $k' = 4.4$). Hydraulic permeabilities were analyzed in terms of Darcy's law [68]

$$K_D = \frac{u_{sf} L_{bed} \eta}{\Delta p} \quad \text{or} \quad \frac{\Delta p}{L_{bed}} = \frac{\eta}{K_D} u_{sf}, \tag{2}$$

where Δp is the pressure drop across a monolithic bed of length L_{bed}, u_{sf} is the superficial velocity determined as the volumetric flow rate over the (empty) cross-sectional area of the analytical column, η is the mobile phase viscosity, and K_D is the Darcy permeability. The mobile phase viscosity for the water/ACN 40/60 (v/v) mobile phase is $\eta = 7.5 \times 10^{-4}$ kg m^{-1} s^{-1} at $T = 298$ K and $p = 0.1$ MPa [69]. The pressure gradient $\Delta p/L_{bed}$ as a function of the superficial velocity u_{sf} is plotted for both monolith generations in Fig. 1. Data were subjected to a linear fit through the origin. The slope m of the linear fitting functions in Fig. 1 can be readily translated into permeability with Eq. (2) by $K_D = \eta/m$. According to the respective pressure drop–flow rate behavior in Fig. 1, the 2nd generation Chromolith column has a 64% lower Darcy permeability than its predecessor ($K_D = 2.68 \times 10^{-14}$ m^2 vs. 7.38×10^{-14} m^2). This observation points to a reduced macropore size in the 2nd generation monoliths. Although reducing the permeability is undesirable, this feature does not seriously compromise column performance, because the permeability is still well above those of particulate packings obtained with modern fine (*e.g.*, sub-3 μm shell and fully porous sub-2 μm) particles [70] and does not threaten to reach the equipment's back pressure limit. For example, if we estimate the equivalent permeability particle diameter ($d_{p,perm}$) of particle-packed beds for the monolith permeability data in Fig. 1, assuming an external (interparticle) porosity of the particulate beds of $\varepsilon_{ext} = 0.366$, with the Kozeny–Carman equation [71]

$$u_{sf} = \frac{d_{p,perm}^2}{180} \frac{\varepsilon_{ext}^3}{\eta(1-\varepsilon_{ext})^2} \frac{\Delta p}{L_{bed}}, \tag{3}$$

we obtain $d_{p,perm} \sim 10$ μm for the 1st generation monoliths, in very good agreement with earlier analysis [17,20], and $d_{p,perm} \sim 6$ μm for the 2nd generation monoliths. The permeability of the 2nd generation monoliths is thus equivalent to that of a packed bed of 6 μm particles at the assumed bed porosity ($\varepsilon_{ext} = 0.366$).

Fig. 2 illuminates the separation efficiency of the two Chromolith generations. Fig. 2A shows chromatograms for butylbenzene acquired at a volumetric flow rate of 2.4 mL/min. The surface chemistry has not changed in the new Chromolith generation, as we ascertained by recording the retention factor of butylbenzene over the whole range of flow velocities and finding no significant difference between the two columns (data not shown). While the retention time is nearly unchanged, peak width and shape are visibly improved in the 2nd generation columns. Both peaks show tailing, but the peak symmetry improves by 25% between the 1st and 2nd generation Chromolith columns (Table 1). Although undesired peak broadening and tailing in chromatography may also be caused by the heterogenous mass transfer kinetics associated with surface heterogeneity [72], the essentially identical surface chemistry of the two monolith generations points to radial morphological heterogeneity as the causative agent for the peak asymmetry of the 1st generation column: if morphological parameters such as the local macroporosity or the macropore size, for example, vary between edge and center of a column, a velocity and transport gradient across the column radius results. Lateral equilibration between center and edge of a column is mainly driven by diffusion [29], which is a slow process compared to the longitudinal flow velocity of the mobile phase. To achieve complete lateral equilibration over the column radius, the column length needs to be sufficient [73]. For columns above capillary format, as in the present analytical monoliths, this condition is not met, and a radial morphology gradient will therefore yield asymmetric peaks. Fig. 2B and C presents plate height curves (plate height H vs. average velocity u_{av}) determined from the butylbenzene peak, but in different ways: Fig. 2B relies on the conventional analysis of measuring the full width at half maximum (FWHM) of the peak, whereas the data in Fig. 2C were determined from the peak's statistical moments after numerical integration of the baseline-corrected peaks and also by accounting for extra-column effects [62]:

$$H = L_{bed} \frac{\mu_2' - \mu_{2,extra}'}{(\mu_1 - \mu_{1,extra})^2}. \tag{4}$$

Here, μ_1 is the overall (system and column) first central moment of the concentration profile, μ'_2 is the overall second central moment of the concentration profile, $\mu_{1,extra}$ is the first central moment of the corresponding extra-column band profile, and $\mu'_{2,extra}$ is the second central moment of the corresponding extra-column band profile.

Plate height data are usually acquired over a narrow range of velocities, as in Fig. 2. Therefore, the curves in Fig. 2B and C were fitted with the simple van Deemter model [74] to extract the coordinates characterizing the plate height minimum (H_{min} and the associated average velocity, $u_{av,min}$) and retrieve the effect of morphological differences of the monoliths in the individual plate height terms of the van Deemter equation

$$H = A + \frac{B}{u_{av}} + Cu_{av}, \quad (5)$$

where the coefficients A, B, and C characterize, respectively, the contribution of classical eddy dispersion (providing a velocity-independent A-term), longitudinal molecular diffusion, and mass transfer resistances in the mobile and stationary phase [75].

The improved separation efficiency of the 2nd generation Chromolith column is obvious from the vertical distance between the two curves in Fig. 2B. The minimum plate height is reduced by 39% from 1st (H_{min} = 11.0 μm) to 2nd generation monolith (H_{min} = 6.7 μm), while the flow velocity associated with the minimum plate height remains similar (1.76 vs. 1.91 mm/s; Table 1). Also recognizable is the smaller slope at higher flow velocities of the 2nd generation column, although the slope observed for silica monoliths is generally shallow compared with particulate columns [76]. Because the FWHM-based method does not consider the full peak area, peak tailing has little effect on the resulting plate height curves. In contrast, the plate height curves in Fig. 2C reflect the full peak area, so that minor differences between individual chromatograms have more influence on the plate height data, which explains the higher data scatter in Fig. 2C compared with Fig. 2B. But the method of statistical moments yields more accurate plate height data than methods that use selected peak parameters or rely on fitting the peak to a predefined functional shape [62,63]. By taking full account of the asymmetric peak shape of the 1st generation Chromolith column (Fig. 2A), the data in Fig. 2C reveal the true extent of the separation efficiency improvement achieved with the 2nd generation Chromolith column: a 66.5% reduction in minimum plate height (from H_{min} = 21.8 μm to 7.3 μm) and a more than 3-fold increase of the minimum velocity (from $u_{av,min}$ = 0.50 mm/s to 1.79 mm/s; Table 1). The difference between the plate height curves of Fig. 2B and C proves that the reduced peak asymmetry of the 2nd generation Chromolith column is a major factor for its enhanced separation efficiency, and this, in turn, indicates a monolith morphology with less radial heterogeneity.

The results for the coefficients in the van Deemter equation (Eq. (5)) are also summarized in Table 1. They similarly indicate a major reduction of the eddy dispersion contribution (A-term) for the 2nd generation Chromolith column: by 61% for the FWHM-based method, and by even 76.5% when the plate height data based on the statistical moments of the peaks are used for analysis. Whereas the data in Fig. 2B are indifferent concerning B-term and C-term contributions for the two monolith generations (Table 1), Fig. 2C suggests a reduction of the C-term for the 2nd generation Chromolith column by 81%, but the B-term simultaneously increases by a factor of ~2.4. This is surprising and is probably caused by the insufficient data available at low velocities ($u_{av} < u_{av,min}$ in Fig. 2C) as well as the general scatter in the data. Overall, the results obtained with the van Deemter equation prove a strong reduction of eddy dispersion in the 2nd generation Chromolith columns. However, this analysis also shows that a definite assignment of the dramatic improvement to a particular morphological property as well as a clear distinction between the individual terms in Eq. (5) is impossible. Thus, the information and insight gained from the popular van Deemter plate height analysis remains limited [77,78]. More sophisticated, quantitative approaches are required to correlate the separation efficiency with the morphology.

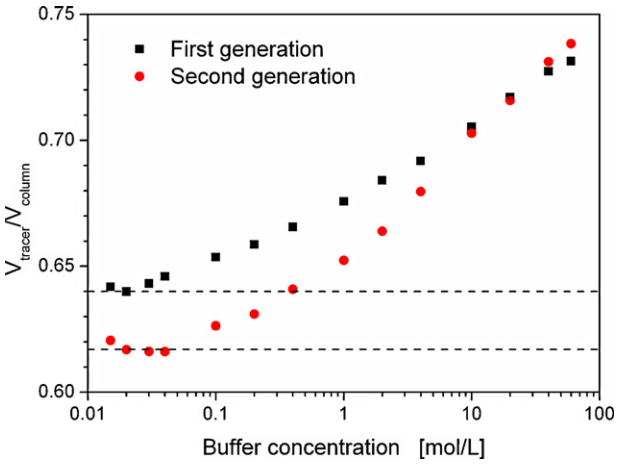

Fig. 3. Electrostatic (Donnan) exclusion chromatography with 1st and 2nd generation Chromolith columns (4.6 mm × 100 mm, C_{18}-modified, fully end-capped). Mobile phase: 50/50 (v/v) water/ACN containing Tris–HCl buffer (pH 8.1) at the indicated concentration, analyte:KNO_3. Dashed lines mark the plateau region indicating the external or macroporosity ($V_{inter}/V_{column} = \varepsilon_{ext}$).

3.2. Porosity of analytical Chromolith columns

The external or macroporosity ε_{ext} of the analytical Chromolith columns was determined by electrostatic (Donnan) exclusion chromatography. This technique makes use of the residual surface silanol groups that are dissociated in contact with an electrolyte-containing mobile phase of pH > 8, resulting in a defined electrical double layer at the silica surface. Varying the mobile phase ionic strength controls the double layer thickness and thus the extent of Donnan exclusion of a co-ionic analyte (*e.g.*, the nitrate ions) from the pore space [79], which allows to distinguish between macropores and mesopores (or, for columns packed with porous particles, between external and internal pores) [80,81]. The thin electrostatic double layer that forms at high ionic strength allows a co-ionic tracer to experience the total pore space; with decreasing ionic strength of the eluent, the double layer thickness grows up to a point at which double layer overlap completely excludes the co-ionic tracer from the mesopores, so that the tracer's elution volume reflects the macropore space only. The simple and rapid procedure involved makes electrostatic (Donnan) exclusion chromatography a viable option for porosity-determination, particularly as other established techniques, such as inverse size exclusion chromatography [82], use experimental conditions (eluents and tracers) that differ strongly from those of actual chromatographic analyses.

Fig. 3 shows the electrostatic exclusion curves, the ratio of the co-ionic tracer (nitrate ions) elution volume to total column volume (V_{tracer}/V_{column}) as a function of the Tris–HCl (pH 8.1) buffer concentration in a mobile phase of water/ACN 50/50 (v/v), for the two analytical Chromolith columns. From the plateau region at low buffer concentrations (< 0.04 mol/L), external or macroporosities of ε_{ext} = 0.64 and ε_{ext} = 0.62 were determined for the 1st and 2nd generation Chromolith columns, respectively.

Instead of eluting with high buffer concentrations to reach a second plateau marking a column's total porosity, ε_{tot} was easier obtained using a neutral, unretained analyte with access to the total pore space. The total porosity of both columns was determined as ε_{tot} = 0.81 from the elution volume of thiourea in a mobile phase

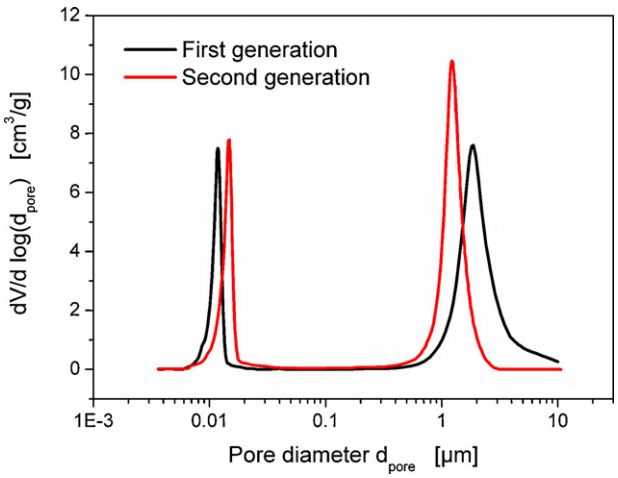

Fig. 4. Bimodal pore size distribution of bare-silica rods (4.6 mm × 150 mm) from the 1st and 2nd Chromolith generation determined by mercury intrusion porosimetry.

of water/ACN 20/80 (v/v) at a flow rate of 0.5 mL/min. Using the relation

$$\varepsilon_{tot} = \varepsilon_{ext} + \varepsilon_{int,col}, \quad (6)$$

which defines the internal porosity as the fraction of column volume occupied by the mesopores, the column internal porosities for the 1st and 2nd generation Chromolith columns were calculated as $\varepsilon_{int,col} = 0.17$ and $\varepsilon_{int,col} = 0.19$, respectively. An alternative definition of the internal porosity ($\varepsilon_{int,skel}$) relates the mesopore fraction to the volume of the silica skeleton, similar to particulate beds, where the internal porosity is calculated as the void volume fraction of the volume occupied by the porous silica particles. Using the relation

$$\varepsilon_{tot} = \varepsilon_{ext} + (1 - \varepsilon_{ext})\varepsilon_{int,skel}, \quad (7)$$

the skeleton internal porosities for the 1st and 2nd generation Chromolith columns were calculated as $\varepsilon_{int,skel} = 0.47$ and $\varepsilon_{int,skel} = 0.50$, respectively. Thus, in terms of porosities (Table 1), the two Chromolith generations are very similar and display values common to silica monoliths [82].

3.3. Pore size distributions, pore volumes, and surface area of bare-silica Chromolith rods

The monoliths' meso- and macropores size distributions (Fig. 4) and associated pore volume fractions as well as the surface area were determined by MIP (Table 2). Fig. 4 shows the monoliths' bimodal pore size distribution, for which mesopore and macropore sizes were measured in the range of 3.7–190 nm and 0.2–10 μm, respectively. Mesopores are shifted towards larger values, from an average size of 11.8 to 14.7 nm, in the 2nd generation Chromolith column, but the width of the curve remains the same. In contrast, the macropore size distribution is visibly narrowed for the 2nd generation Chromolith column, as well as shifted to smaller values, which corresponds to a 34% reduction of average macropore size from 1.86 to 1.23 μm.

In accordance with the changes in porosity (Section 3.2) and average pore size, the mesopore volume is increased (from 0.726 to 0.902 cm^3/g) and the macropore volume decreased (from 2.332 to 2.150 cm^3/g) in the 2nd generation columns, whereas the total pore volume is the same for both monolith generations. A more than threefold increase in macropore surface area (from 2.3 to 7.5 m^2/g) between the two monolith generations has no impact on the total surface area, because the mesopore surface area, which constitutes > 97% of the total surface area, is practically unchanged.

In summary, the conservation of porosities, total pore volume, and mesopore and total surface area between the two Chromolith generations explains the unaltered retention properties observed in Section 3.1, while the decreased average value and width of the macropore size distribution for the 2nd generation Chromolith column agrees with the observed lower hydraulic permeability (to which also the slightly lower macroporosity contributes) and enhanced separation efficiency.

3.4. Scanning electron microcopy of bare-silica Chromolith rods

To investigate the morphology of the two Chromolith generations, we used bare-silica rods instead of the finished product, the PEEK-clad analytical columns. These rods possess the same morphology as the final Chromolith columns, but not the surface modifications and PEEK-tubing that would be obstructive to SEM and CLSM experiments. A first assessment of the morphology was made on the basis of SEM images. For image acquisition, the bare-silica rods were broken at arbitrary intervals rather than cut, to avoid alterations of the surface area caused by abrasion. The fractionated, clean surfaces of the monolithic material were imaged directly, without sputter coating, as this procedure yielded optimal image quality using the microscope's lower secondary electron image mode.

Fig. 5 compares micrographs of the two Chromolith generations at magnifications of 2000:1 (top row) and 5000:1 (bottom row). The morphology of the 2nd generation monolith (right) appears as a denser structure, made up of a finer skeleton and laced with a larger number of smaller macropores. Based on five micrographs for each monolith rod, *i.e.*, sampling information from five different positions over the rod's cross-section to evade local inhomogeneities, we measured 140 values each for skeleton thickness and macropore size; the resulting histograms (bin size: 0.25 μm) are shown in Fig. 6.

In accordance with the MIP results, the macropore size distribution for the 2nd generation monolith is narrowed and shifted towards smaller values. The mean values calculated from the histograms reveal a 33% decrease (from 1.98 ± 0.76 μm to 1.33 ± 0.48 μm) in average macropore size between the Chromolith generations (Table 3). The values determined for the average macropore size differ slightly from those obtained by MIP (Table 2), but the relative change between the monolith generations is very similar for SEM and MIP. Small deviations are unsurprising given the drawbacks of both methods. SEM images lack depth

Table 2
Average pore sizes, volumes, and surface areas determined with mercury intrusion porosimetry for bare-silica rods from the 1st and 2nd generation of analytical silica monoliths.

	Average size (μm)			Volume (cm^3/g)			Surface area (m^2/g)		
	1st	2nd	Ratio	1st	2nd	Ratio	1st	2nd	Ratio
Mesopores	0.0118	0.0147	1.25	0.726	0.902	1.24	259.6	257.8	0.99
Macropores	1.86	1.23	0.66	2.332	2.150	0.92	2.3	7.5	3.26
Total	–	–	–	3.058	3.057	1.00	264.8	265.3	1.00

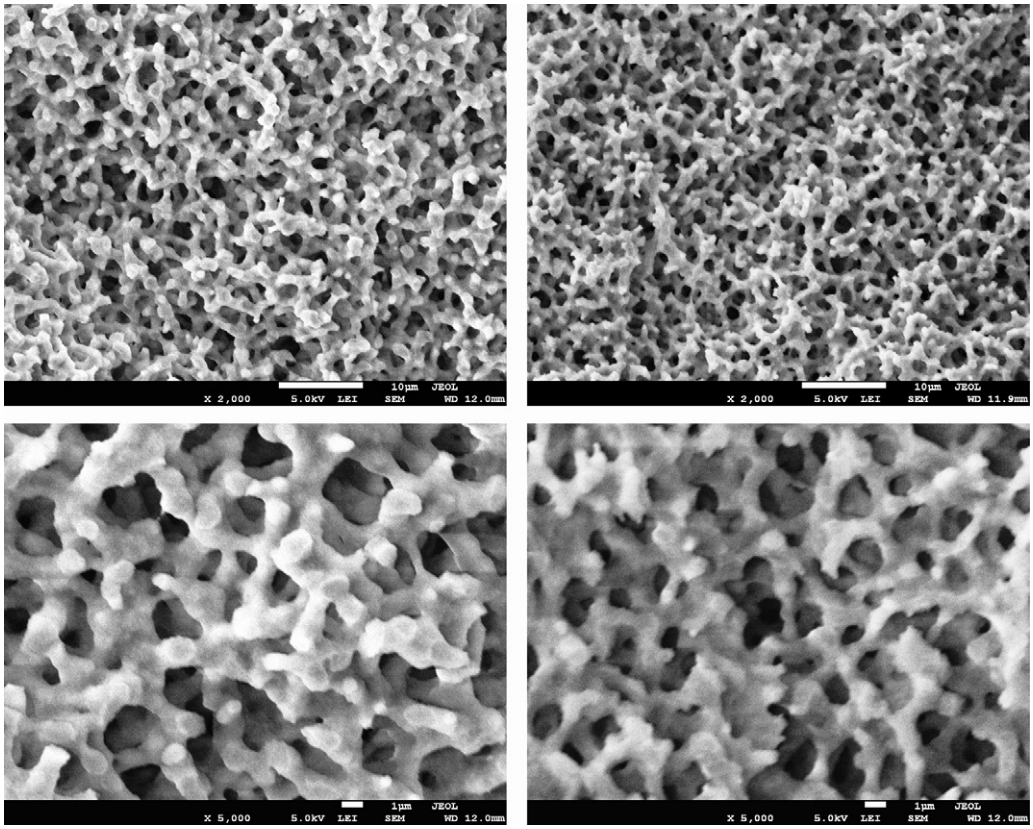

Fig. 5. SEM images of bare-silica rods (4.6 mm × 150 mm) from the 1st (left) and 2nd (right) Chromolith generation at 2000:1 (top) and 5000:1 (bottom) magnification.

information required for a proper segmentation into foreground and background, *i.e.*, skeleton and void space. Determination of macropore sizes by SEM suffers from the ill-defined border between skeleton and void space as well as from the unavoidable bias introduced by the user's selection of macropores for measurement in a SEM image. Also, the column is only locally probed by selected SEM images, whereas MIP explores the whole column. On the other hand, pore size determination from MIP data is based on the assumption of cylindrical pore shape, which may be more or less true for a given sample. MIP is also known to underestimate the pore size, because the acquired data actually reflect the pore entrance, whose diameter may be considerably smaller than those of the pore (so-called ink-bottle effect) [83]. For our two Chromolith samples, MIP and SEM show good agreement in the trends

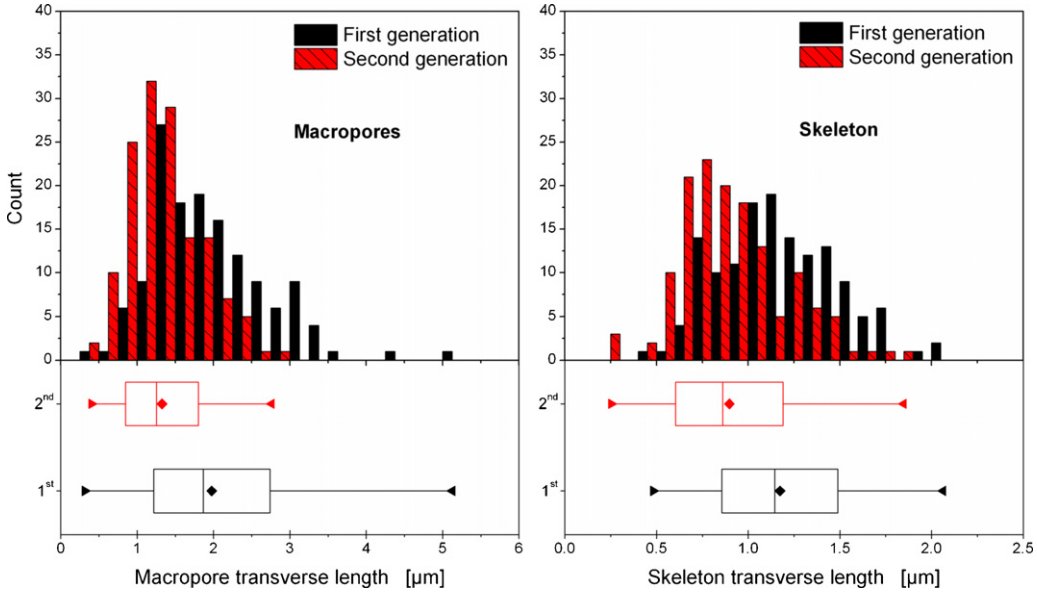

Fig. 6. Histograms for macropore size (left) and skeleton thickness (right) as estimated from SEM images of bare-silica rods (4.6 mm × 150 mm) from the 1st and 2nd Chromolith generation. Box plots summarize statistical parameters: (♦) denotes the mean, the box denotes the median and standard deviation; the whiskers mark the minimum and maximum.

Table 3
Macropore size, skeleton thickness, and domain size as estimated from scanning electron microscopy images of bare-silica rods from the 1st and 2nd generation of analytical silica monoliths.[a]

	1st	2nd	Ratio
Macropore size (μm)	1.98 ± 0.76	1.33 ± 0.48	0.67
Skeleton thickness (μm)	1.17 ± 0.32	0.90 ± 0.29	0.77
Domain size (μm)	3.15	2.23	0.71

[a] Each value is calculated from 140 distance measurements.

they predict for the macropores' average size and width of the size distribution.

Additional morphological information from the SEM images comes for the skeleton: Fig. 6 (right panel) reveals a 23% reduction of average skeleton thickness, from 1.17 ± 0.32 μm to 0.90 ± 0.29 μm, between the monolith generations. Combined, the SEM data for macropore size and skeleton thickness estimate that the domain size, *i.e.*, the sum of average macropore size and average skeleton thickness, was reduced by ~1 μm (from 3.15 to 2.23 μm) in the 2nd generation monoliths. With their smaller domain size, 2nd generation monoliths approach the regime of sub-2 μm particles.

3.5. Confocal laser scanning microscopy of bare-silica Chromolith rods

For a quantitative distinction between 1st and 2nd generation Chromolith morphology, we used cylindrical disks of 1–1.5 mm thickness as sample for each Chromolith generation. The samples were cut orthogonal to the rod axis at *ca.* mid-length of the bare-silica monoliths (Fig. 7). After staining the disks with fluorescent dye, three positions were arbitrarily chosen on each disk, where stacks of CLSM images were acquired and processed with our method. Fig. 8 shows a CLSM image (one optical slice of a stack) after image restoration (Fig. 8A) and after segmentation (Fig. 8B) for each Chromolith generation. The entire silica skeleton is well illuminated, because the fluorophore was able to enter the mesopores and access the center of the skeleton branches. Each image stack represents a physical volume of at least 60 μm × 60 μm × 12.6 μm (Fig. 8C). The physical reconstruction yields a true, three-dimensional representation of the macromorphology, where the evolution between the two Chromolith generations – from coarser to finer and denser structure and from larger to smaller macropores – is clearly recognizable.

The quantitative morphological information contained in the segmented image stacks was extracted in form of chord length distributions (CLDs) [39]. CLD analysis is a statistical method that can be used to describe the void as well as the solid space of porous media. The method is simple: chords are generated by randomly choosing points, for example in the void space, and projecting pairs of opposing vectors from this point in several directions until they strike solid space; vectors projecting out of the image border are discarded. The distance spanned by a vector pair is a chord length. Chords are generated and measured until the resulting distribution is constant. CLD analysis makes no assumptions about the shape of the investigated space. This is a distinct advantage over methods that rely on a presumed geometry and whose results are affected by the difference between assumed and true shape; such methods are never as accurate as CLD analysis. CLD analysis is by no means limited to CLSM images, but applicable to any porous medium representation that provides segmented information. In connection with chromatographic beds, CLD analysis has successfully been used to describe quantitatively the morphology of silica monoliths [34,39,59], polymer monoliths [39], and particulate packings [60].

Table 4
Parameters describing the macromorphology of the 1st and 2nd generation of analytical silica monoliths. The data were extracted from three CLSM image stacks[a] representing each a physical volume of at least 60 μm × 60 μm × 12.6 μm.

	1st	Average	2nd	Average	Ratio
μ_{macro} (μm)	4.79 4.76 4.71	4.75	3.25 3.29 3.33	3.29	0.69
k_{macro}	2.65 2.68 2.71	2.68	2.91 2.89 2.89	2.90	1.08
μ_{skel} (μm)	2.08 2.11 2.10	2.10	1.57 1.59 1.59	1.58	0.75
k_{skel}	3.95 3.96 3.89	3.93	3.43 3.33 3.36	3.37	0.86
ε_{ext}	0.664 0.662 0.661	0.662	0.652 0.656 0.651	0.653	0.99

[a] Image stacks were acquired at three randomly chosen lateral positions of the sample slice cut from the monolithic bare-silica rod.

The CLDs of void and solid space, macropores and skeleton, respectively, are well described by a two parameter k,Γ-function

$$f(l_{chord}) = \frac{k^k}{\Gamma(k)} \frac{l_{chord}^{k-1}}{\mu^k} \exp\left(-k\frac{l_{chord}}{\mu}\right), \quad (8)$$

where l_{chord} denotes chord length, μ is the mean chord length as a first-moment parameter of location of the distribution, $k = \mu^2/\sigma^2$ (where σ is the standard deviation of the CLD) is a second-moment parameter defining the statistical dispersion of the distribution function, and $\Gamma(k)$ is the gamma function. The parameter k relates the variation of the CLD to its average value. k has emerged as a descriptor for the structural homogeneity, with larger values of k indicating more homogeneous structures [34,60,84].

To ensure that the morphological data gathered from the image stacks were representative, we evaluated the influence of the stack dimensions on the resulting CLD as well as the stack-to-stack variation for a given disk sample. We found that the CLDs have converged for lateral dimensions of 2000 × 2000 pixels and axial dimensions of 100 slices, so that the volumes of the acquired image stacks were more than sufficient. Differences in the values for the parameters μ and k of skeleton and macropore CLDs as well as the macroporosity (ε_{ext}), calculated as the fraction of void pixels in an image stack, were observed for the third digit only, which means that stack-to-stack variation is negligible (Table 4).

Fig. 9 compares the two Chromolith generations by their k,Γ-functions fitted to the CLDs determined for macropores (Fig. 9A) and skeleton (Fig. 9B). For both structural features, the CLDs of the 2nd generation monoliths are shifted to smaller values of l_{chord}. The difference between the two Chromolith generations is larger for the macropore space (Table 4): the first moment of the CLD decreases by 31% from μ_{macro} = 4.75 μm to 3.29 μm between 1st and 2nd generation, and the parameter k increases by 8% from k_{macro} = 2.68 to 2.90. The latter indicates a more homogeneous macropore space for the 2nd generation Chromolith, which reduces the velocity bias between neighboring flow channels and thus the short-range interchannel contribution to eddy dispersion [34].

The parameter μ_{macro} represents the mean chord length of the macropore space, not the average macropore diameter. The latter implies a void space of well-defined, cylindrical pores, where the diameter of each macropore could be determined and the average calculated. But this concept is hardly applicable to silica monoliths. Imagining the macropore space as similar to the external pore space of packed beds may be intuitive to chromatographers

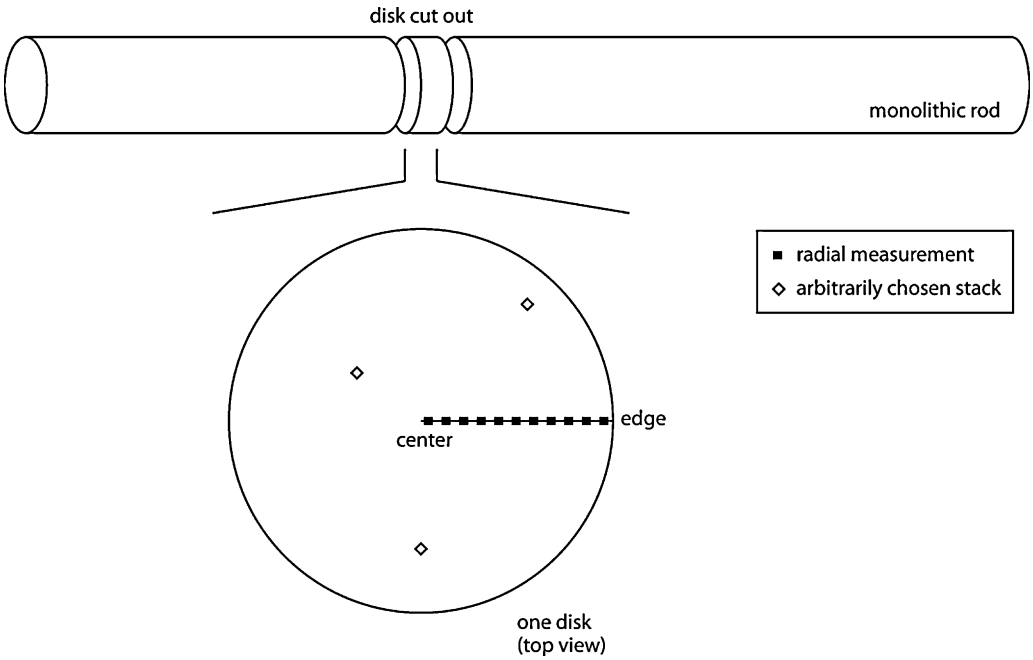

Fig. 7. Scheme illustrating the collection of CLSM data. A slice of ~1 mm thickness was cut at *ca.* mid-length from a bare-silica monolith rod (4.6 mm × 150 mm). Image stacks were acquired at three different lateral positions of the disk to assess general morphological properties. To investigate the radial morphological heterogeneity, a series of image stacks was acquired over the disk radius (from the center to close to the edge) at constant depth.

due to their longstanding experience with particulate adsorbents, but is not helpful for interpretation of the macropore CLD, which delivers a quantitative description of monolith morphology in an abstract, but accurate way. Although μ_{macro} should not be confused with the average macropore size, reduction of either parameter means a shortened lateral distance for the tracer to cover in the mobile phase between two encounters with the skeleton. This lowers the transchannel contribution to eddy dispersion, which results from the flow velocity bias over the largest lateral distance across a pore [26,34]. (In the van Deemter model, the shortened lateral distance across the pores would count as a reduced contribution from mass transfer resistance in the mobile phase, *i.e.*, as part of the C-term in Eq. (5).)

Another benefit for the separation efficiency of the 2nd generation Chromolith is the 25% reduction of the mean skeleton chord length, from μ_{skel} = 2.10 μm to 1.58 μm, observed for the skeleton CLD (Fig. 9B and Table 4). A thinner skeleton reduces the transskeleton contribution to eddy dispersion, because if the distance an analyte has to cover by diffusion is shortened, the respective velocity bias decreases. The reduced skeleton thickness comes at the cost

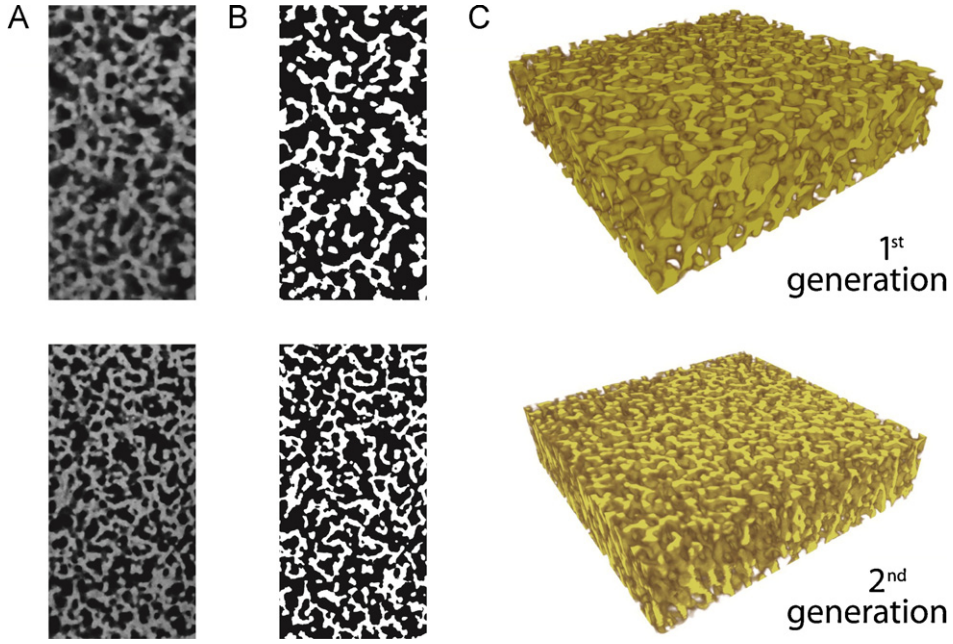

Fig. 8. (A) Fully restored CLSM images (optical slice) of bare-silica rods from the 1st (top) and 2nd (bottom) Chromolith generation. (B) The images after segmentation. (C) Macromorphology of the 1st and 2nd Chromolith generation as physically reconstructed from two CLSM image stacks each representing a physical volume of 60 μm × 60 μm × 12.6 μm.

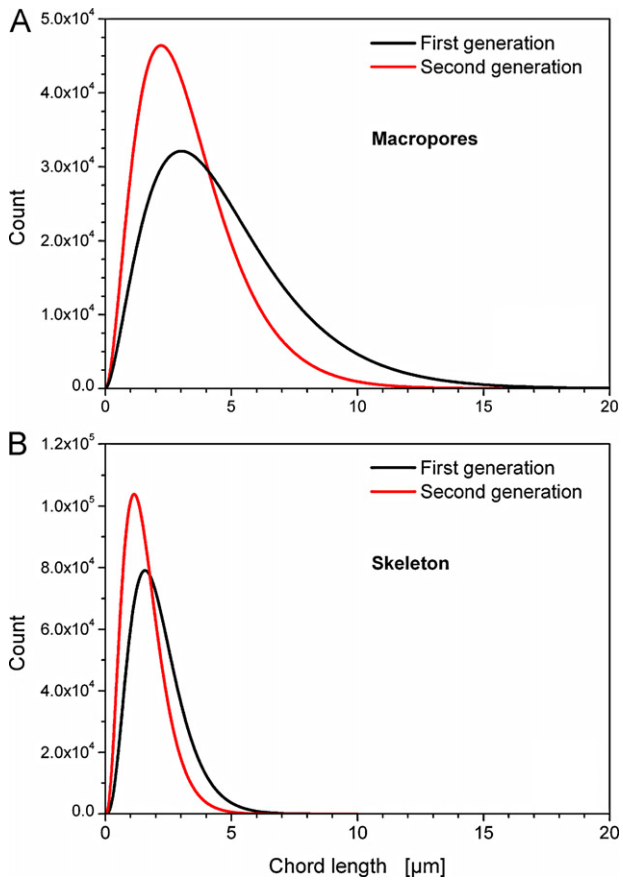

Fig. 9. k-gamma fit of the chord length distributions for macropore space (A) and silica skeleton (B) in the 1st and 2nd Chromolith generation. The distributions represent chord lengths from one image stack in each case.

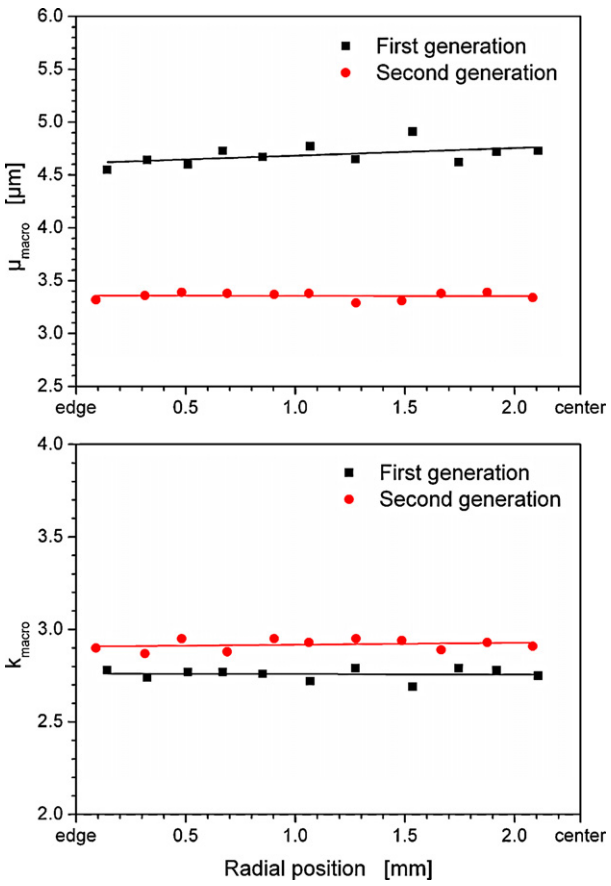

Fig. 10. Radial variation of macropore properties in the 1st and 2nd Chromolith generation as described by μ_{macro} (top) and k_{macro} (bottom). Linear fits to the data are shown as a guide to the eye.

of a decreased parameter k_{skel}, from k_{skel} = 3.93 to 3.37, but this loss of skeleton size homogeneity has little effect on the overall separation efficiency of the 2nd generation Chromolith columns. Covering a wide range of analyte and skeleton properties (values of the diffusion coefficient as well as skeleton porosity and tortuosity), it has been demonstrated that the role of transport properties inside the monolith skeleton can be neglected compared with eddy dispersion that originates in the monolith's macropore space [85].

So far, CLD analysis of the monoliths' macromorphology reconstructed by CLSM has revealed that the 2nd generation Chromolith rods have smaller macropore dimensions, a more homogeneous macropore space over short-range distances, and a thinner silica skeleton, which would reduce the transchannel, the short-range interchannel, and the transskeleton contributions to eddy dispersion, respectively, and thus improve a column's separation efficiency. If we compare CLSM and SEM results, there is excellent agreement for the relative changes in macropore space and silica skeleton between the two monolith generations: SEM estimates a 33% reduction of average macropore size and a 23% reduction of average skeleton thickness, and CLSM yields a 31% and 25% reduction for μ_{macro} and μ_{skel}, respectively. Despite its shortcomings, SEM has predicted two of the relevant changes with remarkable accuracy; this success certainly owes to the number of data extracted manually from the SEM images. Extracting quantitative values for the homogeneity of a morphological property comparable to k_{skel} and k_{macro} from SEM data, however, is beyond the method's capabilities.

An important aspect of column morphology, for whose evaluation CLSM is ideally suited, is the radial variation of the monolith structure. Often named as their major drawback, radial heterogeneity can take different forms in silica monoliths [4], but always increases the transcolumn contribution to eddy dispersion. Gaps between column wall and monolithic packing are the most serious form of radial heterogeneity, often causing a dramatic loss of separation efficiency. Large gaps such as observed for capillary silica monoliths [29,34] are improbable for larger column formats, because the dried (and shrank) monolithic rod is tightly wrapped into the tubing in the last stages of column production. Aging may shrink a clad silica monolithic bed subtly over time, so that wall defects – although smaller in dimension and effect as in the capillary format – are also possible in larger-diameter columns. However, such wall defects occur sporadically along the length of the PEEK-clad column. The radial heterogeneity we investigate with the CLSM method refers to a systematic difference in morphological properties over the radius of the monolithic silica rod present over the whole rod length and indicative of a specific preparation method or monolith generation.

To investigate the radial heterogeneity of the analytical silica monoliths, we reconstructed the macromorphology at 11 radial positions of a disk sample (Fig. 7), starting close to the edge and moving towards the center, in intervals of *ca.* 200 µm, while maintaining the same vertical position in a disk to focus on radial rather than on longitudinal heterogeneity. The reconstructed volumes were subjected to CLD analysis of skeleton and macropore space, extracting the parameters μ and k from each CLD. Figs. 10 and 11 compare the two silica monolith generations with respect to the radial homogeneity of macropore space and silica skeleton, respectively. In the 2nd generation monolith, the macropore space is remarkably invariant over the disk radius (Fig. 10), whereas the 1st generation monolith shows a small increase of μ_{macro} from

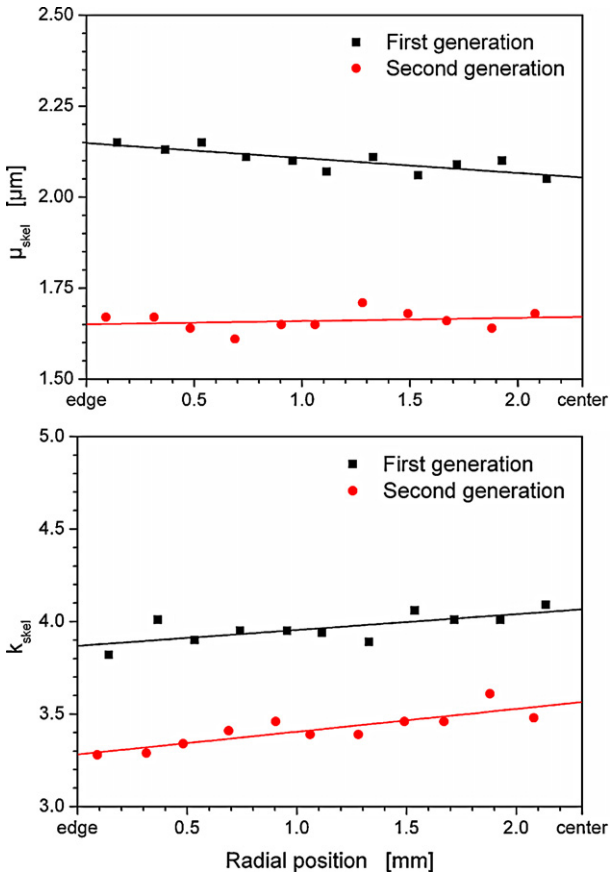

Fig. 11. Radial variation of skeleton properties in the 1st and 2nd Chromolith generation as described by μ_{skel} (top) and k_{skel} (bottom). Linear fits to the data are shown as a guide to the eye.

edge to center at constant k_{macro}. Compared with the values for the macropore space, the data for the silica skeleton (Fig. 11) are more scattered. The mean skeleton chord length μ_{skel} drops slightly from edge to center in the 1st generation Chromolith, but stays fairly constant in the 2nd generation Chromolith. In both monolith generations k_{skel} grows slightly towards the center, *i.e.*, skeleton size homogeneity decreases somewhat towards the edge.

To complement the results with an additional morphological parameter, we monitored the radial dependence of the macroporosity ε_{ext}. Fig. 12 shows no systematic radial dependence of

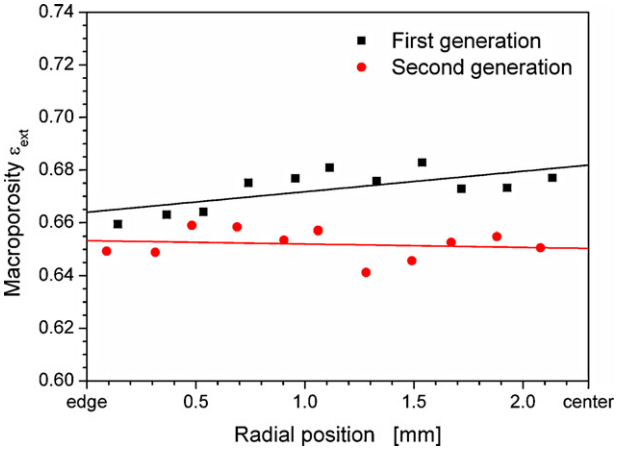

Fig. 12. Radial variation of macroporosity ε_{ext} in the 1st and 2nd Chromolith generation. Linear fits to the data are shown as a guide to the eye.

ε_{ext} for the 2nd generation Chromolith, but a rising edge-to-center gradient of ε_{ext} for the 1st generation Chromolith. The latter observation agrees with the image of growing macropores and a thinning skeleton towards the center of the rod derived from Fig. 10 (μ_{macro}) and Fig. 11 (μ_{skel}). The results of our CLSM investigation describe for the 1st generation monolith a morphological gradient that is opposite to what has been assumed for analytical silica monoliths based on the fact that such columns have a higher permeability near the wall than at the core [28]. The seemingly contradictory statements are not mutually exclusive, however. Our CLSM method sensitively probes the variance of morphological parameters at short intervals (~200 µm distance) over the radius of an unclad silica monolithic rod, starting near the edge, but not at the edge. Guiochon's group investigated PEEK-clad silica monoliths at the column exit, using a detection point close to the actual column wall. One or several small gaps or locally enlarged macropores at the column wall (caused by inelastic deformations of the silica layer close to the wall) could account for the permeability difference between wall and core, even though the general radial morphological gradient of the monolithic rod runs in the opposite direction, *i.e.*, towards slightly larger pores and higher macroporosity in the core. Although the outcome is the same – radial heterogeneity always raises the transcolumn contribution to eddy dispersion and thus lowers separation efficiency – it can occur at different length scales and stem from different sources; to characterize and distinguish between the different causes and forms of radial heterogeneity a combination of methods is needed.

In summary, probing the radial dependence of morphological properties in the two generations of analytical silica monoliths has revealed that except for the skeleton size homogeneity, the macromorphology was substantially improved over the whole column radius in the 2nd generation. The radial homogeneity of μ_{macro}, μ_{skel}, k_{macro}, and ε_{ext} observed for the 2nd generation monoliths explains why the butylbenzene peak (Fig. 2A) has shed much of the asymmetry compared with the 1st generation. If we compare the plate height curves in Fig. 2B (calculated from the peak width at half maximum) and Fig. 2C (calculated from the whole peak area), the large impact of the peak shape on the plate height data is immediately apparent; the elimination of radial heterogeneity in the 2nd generation monoliths is therefore a key factor to their improved separation efficiency.

4. Conclusions

We have presented a comprehensive comparison of analytical silica monoliths from the previous and the coming Chromolith generation, focusing on the relation between monolith morphology and chromatographic performance. Between the two generations of silica monoliths, the surface chemistry, the total surface area, and the total pore volume have not changed, and the porosities (macro-, meso-, total) are also very similar, which guarantees conserved retention properties. The 2nd generation of analytical silica monoliths boasts a substantially improved column performance, characterized by a 66.5% reduction of the minimum plate height and a 3.6-fold increase of the corresponding flow velocity. This improvement in separation efficiency originates from several advances in monolith morphology that reduce the eddy dispersion contribution to band broadening at various length scales: a smaller macropore size and thinner skeleton lower the transchannel and the transskeleton contribution, respectively, and a more homogeneous macropore space at short distances as well as over the column radius reduces the short-range interchannel and the transcolumn contribution. In essence, the domain size was decreased by *ca.* 29% in the 2nd generation of silica monoliths, while radial heterogeneity was eliminated for the macropore space

and for the average skeleton thickness. The successful attempt to simultaneously shrink the domain size and improve the structural homogeneity is a breakthrough, proving that higher structural homogeneity is possible with smaller domain sizes. As a consequence, the new generation of analytical silica monoliths is much better equipped to compete with the newer developments in particle technology.

This work also shows that the combination of CLSM-based imaging and statistical analysis methods enables new insights into the column morphology, which not only guide a detailed explanation of the chromatographic performance, but also provide vital clues for silica monolith preparation; the morphological information derived from the CLSM-investigated slices allowed us to identify the relevant structural elements behind the improved separation efficiency of the 2nd generation analytical silica monoliths.

The consequences of the improved morphology of the 2nd generation Chromolith for eddy dispersion could be quantified by using the reconstructions from the two monolith generations (Fig. 8C) as benchmark in numerical simulations of flow and mass transport, as demonstrated recently with capillary silica monoliths [29,85,86].

Acknowledgements

This work was supported by the Deutsche Forschungsgemeinschaft DFG (Bonn, Germany) under grant TA 268/6-1. Laboratory samples of 1st and 2nd generation Chromolith columns were kindly provided by Merck Millipore (Darmstadt, Germany). We thank Martin Kollmann and Professor Joachim Schachtner (Department of Biology, Philipps-Universität Marburg) for their help with the CLSM measurements and Dr. Stephan Altmaier from Merck Millipore for the MIP data.

References

[1] F. Svec, C.G. Huber, Anal. Chem. 78 (2006) 2100.
[2] H. Kobayashi, T. Ikegami, H. Kimura, T. Hara, D. Tokuda, N. Tanaka, Anal. Sci. 22 (2006) 491.
[3] K. Nakanishi, N. Tanaka, Acc. Chem. Res. 40 (2007) 863.
[4] G. Guiochon, J. Chromatogr. A 1168 (2007) 101.
[5] A. Jungbauer, R. Hahn, J. Chromatogr. A 1184 (2008) 62.
[6] K.K. Unger, R. Skudas, M.M. Schulte, J. Chromatogr. A 1184 (2008) 393.
[7] O. Núñez, K. Nakanishi, N. Tanaka, J. Chromatogr. A 1191 (2008) 231.
[8] J. Urban, P. Jandera, J. Sep. Sci. 31 (2008) 2521.
[9] A. Nordborg, E.F. Hilder, Anal. Bioanal. Chem. 394 (2009) 71.
[10] I. Nischang, O. Brueggemann, F. Svec, Anal. Bioanal. Chem. 397 (2010) 953.
[11] F. Svec, J. Chromatogr. A 1217 (2010) 902.
[12] I. Nischang, I. Teasdale, O. Brüggemann, Anal. Bioanal. Chem. 400 (2011) 2289.
[13] J.J. Kirkland, T.J. Langlois, J.J. DeStefano, Am. Lab. 39 (2007) 18.
[14] G. Guiochon, F. Gritti, J. Chromatogr. A 1218 (2011) 1915.
[15] J.R. Mazzeo, U.D. Neue, M. Kele, R.S. Plumb, Anal. Chem. 77 (2005) 460A.
[16] J.W. Jorgenson, Annu. Rev. Anal. Chem. 3 (2010) 129.
[17] M. Kele, G. Guiochon, J. Chromatogr. A 960 (2002) 19.
[18] F. Gritti, W. Piatkowski, G. Guiochon, J. Chromatogr. A 978 (2002) 81.
[19] U. Tallarek, F.C. Leinweber, A. Seidel-Morgenstern, Chem. Eng. Technol. 25 (2002) 1177.
[20] F.C. Leinweber, U. Tallarek, J. Chromatogr. A 1006 (2003) 207.
[21] F. Gritti, W. Piatkowski, G. Guiochon, J. Chromatogr. A 983 (2003) 51.
[22] A.E. Rodrigues, V.G. Mata, M. Zabka, L. Pais, in: F. Svec, T.B. Tennikova, Z. Deyl (Eds.), Monolithic Materials: Preparation, Properties, and Applications, Journal of Chromatography Library, vol. 67, Elsevier Science B.V., Amsterdam, 2003, p. 325.
[23] K. Cabrera, J. Sep. Sci. 27 (2004) 843.
[24] M. Zabka, M. Minceva, A.E. Rodrigues, J. Biochem. Biophys. Methods 70 (2007) 95.
[25] R. Skudas, B.A. Grimes, M. Thommes, K.K. Unger, J. Chromatogr. A 1216 (2009) 2625.
[26] F. Gritti, G. Guiochon, J. Chromatogr. A 1216 (2009) 4752.
[27] K.S. Mriziq, J.A. Abia, Y. Lee, G. Guiochon, J. Chromatogr. A 1193 (2008) 97.
[28] J.A. Abia, K.S. Mriziq, G.A. Guiochon, J. Chromatogr. A 1216 (2009) 3185.
[29] D. Hlushkou, S. Bruns, A. Höltzel, U. Tallarek, Anal. Chem. 82 (2010) 7150.
[30] K. Kanamori, H. Yonezawa, K. Nakanishi, K. Hirao, H. Jinnai, J. Sep. Sci. 27 (2004) 874.
[31] M. Motokawa, M. Ohira, H. Minakuchi, K. Nakanishi, N. Tanaka, J. Sep. Sci. 29 (2006) 2471.
[32] R. Roux, M. Abi Jaoudé, C. Demesmay, J. Chromatogr. A 1216 (2009) 3857.
[33] T. Hara, S. Makino, Y. Watanabe, T. Ikegami, K. Cabrera, B. Smarsly, N. Tanaka, J. Chromatogr. A 1217 (2010) 89.
[34] S. Bruns, T. Hara, B.M. Smarsly, U. Tallarek, J. Chromatogr. A 1218 (2011) 5187.
[35] H. Minakuchi, K. Nakanishi, N. Soga, N. Ishizuka, N. Tanaka, J. Chromatogr. A 762 (1997) 135.
[36] H. Minakuchi, K. Nakanishi, N. Soga, N. Ishizuka, N. Tanaka, J. Chromatogr. A 797 (1998) 121.
[37] M. Motokawa, H. Kobayashi, N. Ishizuka, H. Minakuchi, K. Nakanishi, H. Jinnai, H. Hosoya, T. Ikegami, N. Tanaka, J. Chromatogr. A 961 (2002) 53.
[38] T. Hara, H. Kobayashi, T. Ikegami, K. Nakanishi, N. Tanaka, Anal. Chem. 78 (2006) 7632.
[39] J. Courtois, M. Szumski, F. Georgsson, K. Irgum, Anal. Chem. 79 (2007) 335.
[40] W. Denk, H. Horstmann, PLoS Biol. 2 (2004) 1900.
[41] H. Reingruber, A. Zankel, C. Mayrhofer, P. Poelt, J. Membr. Sci. 372 (2011) 66.
[42] H. Koku, R.S. Maier, K.J. Czymmek, M.R. Schure, A.M. Lenhoff, J. Chromatogr. A 1218 (2011) 3466.
[43] J.D. Seymour, P.T. Callaghan, AIChE J. 43 (1997) 2096.
[44] U. Tallarek, E. Bayer, D. van Dusschoten, T. Scheenen, H. Van As, G. Guiochon, U.D. Neue, AIChE J. 44 (1998) 1962.
[45] A.J. Sederman, P. Alexander, L.F. Gladden, Powder Technol. 117 (2001) 255.
[46] T. Aste, M. Saadatfar, T.J. Senden, Phys. Rev. E 71 (2005) 061302.
[47] H. Dong, M.J. Blunt, Phys. Rev. E 80 (2009) 036307.
[48] C.J. Gommes, A.-J. Bons, S. Blacher, J.H. Dunsmuir, A.H. Tsou, AIChE J. 55 (2009) 2000.
[49] K. Schladitz, J. Microsc. 243 (2011) 111.
[50] E. Gillespie, D. Connolly, M. Macka, P.N. Nesterenko, B. Paull, Analyst 132 (2007) 1238.
[51] D. Connolly, L.P. Barron, E. Gillespie, B. Paull, Chromatographia 70 (2009) 915.
[52] Z. Walsh, M. Vazquez, F. Benito-Lopez, B. Paull, M. Macka, F. Svec, D. Diamond, Lab Chip 10 (2010) 1777.
[53] S. Wilhelm, B. Gröbler, M. Gluch, H. Heinz, Confocal Laser Scanning Microscopy—Optical Image Formation and Electronic Signal Processing, Monography, Carl Zeiss, Jena, Germany, 2008.
[54] H. Jinnai, K. Nakanishi, Y. Nishikawa, J. Yamanaka, T. Hashimoto, Langmuir 17 (2001) 619.
[55] K. Kanamori, K. Nakanishi, K. Hirao, H. Jinnai, Langmuir 19 (2003) 5581.
[56] H. Saito, K. Kanamori, K. Nakanishi, K. Hirao, Y. Nishikawa, H. Jinnai, Colloids Surf., A 241 (2004) 215.
[57] H. Saito, K. Nakanishi, K. Hirao, H. Jinnai, J. Chromatogr. A 1119 (2006) 95.
[58] H. Saito, K. Kanamori, K. Nakanishi, K. Hirao, Y. Nishikawa, H. Jinnai, Colloids Surf., A 300 (2007) 245.
[59] S. Bruns, T. Müllner, M. Kollmann, J. Schachtner, A. Höltzel, U. Tallarek, Anal. Chem. 82 (2010) 6569.
[60] S. Bruns, U. Tallarek, J. Chromatogr. A 1218 (2011) 1849.
[61] S. Altmaier, K. Cabrera, J. Sep. Sci. 31 (2008) 2551.
[62] F. Gritti, G. Guiochon, J. Chromatogr. A 1218 (2011) 4452.
[63] F. Gritti, G. Guiochon, J. Chromatogr. A 1218 (2011) 5216.
[64] W.S. Rasband, ImageJ, U.S. National Institutes of Health, Bethesda, MD, 1997–2011, http://rsb.info.nih.gov//ij/.
[65] B. Abrams, Z. Diwu, O. Guryev, S. Aleshkov, R. Hingorani, M. Edinger, R. Lee, J. Link, T. Dubrovsky, Anal. Biochem. 386 (2009) 262.
[66] F. Luisier, PureDenoise, Biomedical Imaging Group, École Polytechnique Fédéral de Lausanne, 2010, http://bigwww.epfl.ch/algorithms/denoise.
[67] S. Bochkanov, V. Bystritsky, ALGLIB, www.alglib.net.
[68] D. Hlushkou, U. Tallarek, J. Chromatogr. A 1126 (2006) 70.
[69] J.W. Thompson, T.J. Kaiser, J.W. Jorgenson, J. Chromatogr. A 1134 (2006) 201.
[70] F. Gritti, G. Guiochon, J. Chromatogr. A 1217 (2010) 5069.
[71] F.C. Leinweber, D. Lubda, K. Cabrera, U. Tallarek, Anal. Chem. 74 (2002) 2470.
[72] A. Felinger, J. Chromatogr. A 1126 (2006) 120.
[73] G. Gotmar, T. Fornstedt, G. Guiochon, J. Chromatogr. A 831 (1999) 17.
[74] J.J. van Deemter, F.J. Zuiderweg, A. Klinkenberg, Chem. Eng. Sci. 5 (1956) 271.
[75] J.C. Giddings, Dynamics of Chromatography. Part 1: Principles and Theory, Marcel Dekker, New York, 1965.
[76] A.M. Siouffi, J. Chromatogr. A 1126 (2006) 86.
[77] M.R. Schure, R.S. Maier, D.M. Kroll, H.T. Davis, Anal. Chem. 74 (2002) 6006.
[78] S. Khirevich, A. Höltzel, A. Seidel-Morgenstern, U. Tallarek, Anal. Chem. 81 (2009) 7057.
[79] A. Höltzel, U. Tallarek, J. Sep. Sci. 30 (2007) 1398.
[80] S. Jung, S. Ehlert, M. Pattky, U. Tallarek, J. Chromatogr. A 1217 (2010) 696.
[81] S. Jung, D. Stoeckel, U. Tallarek, J. Sep. Sci. 34 (2011) 800.
[82] M. Al-Bokari, D. Cherrak, G. Guiochon, J. Chromatogr. A 975 (2002) 275.
[83] A.B. Abell, K.L. Willis, D.A. Lange, J. Colloid Interface Sci. 211 (1999) 39.
[84] I. Schenker, F.T. Filser, L.J. Gauckler, T. Aste, H.J. Herrmann, Phys. Rev. E 80 (2009) 021302.
[85] D. Hlushkou, S. Bruns, A. Seidel-Morgenstern, U. Tallarek, J. Sep. Sci. 34 (2011) 2026.
[86] D. Hlushkou, S. Bruns, U. Tallarek, J. Chromatogr. A 1217 (2010) 3674.